ORIGINAL ARTICLE

On the speed of piezostrain-mediated voltage-driven perpendicular magnetization reversal: a computational elastodynamics-micromagnetic phase-field study

Ren-Ci Peng[1], Jia-Mian Hu[2], Long-Qing Chen[1,2] and Ce-Wen Nan[1]

By linking the dynamics of local piezostrain to the dynamics of local magnetization, we computationally analyzed the speed of a recently proposed scheme of piezostrain-mediated perpendicular magnetization reversal driven by a voltage pulse in magnetoelectric heterostructures. We used a model heterostructure consisting of an elliptical ultrathin amorphous $Co_{20}Fe_{60}B_{20}$ on top of a polycrystalline $Pb(Zr,Ti)O_3$ (PZT) thin film. We constructed a diagram showing the speed of perpendicular magnetization reversal as a function of the amplitude of the applied voltage pulse and the stiffness damping coefficient of PZT film. In addition, we investigated the influence of thermal fluctuations on the switching speed. The analyses suggest that the switching time remains well below 10 ns and that the energy dissipation per switching is on the order of femtojoule. The present computational analyses can be generally used to predict the speed of piezostrain-enabled magnetization switching and magnetic domain-wall motion, which critically determines the response time of corresponding piezostrain-enabled spintronic and magnonic devices.

INTRODUCTION

Magnetoelectric coupling in magnetic/dielectric heterostructures enables ultralow-power spintronic devices by using a non-power-dissipating electric field to control the directions and/or the transport of spins.[1–3] One well-pursued scheme is to use an electric field to reverse the magnetization, suggesting applications in magnetic memories[2] and logic gates.[4] However, this is challenging because a time-invariant electric field cannot break the time-reversal symmetry of magnetization.

Many experimental efforts have been made to achieve voltage-driven magnetization reversal through electrically controlled exchange coupling,[5–7] charge/orbital effect[8–10] and/or strain[11–14] across the interface of magnetic/dielectric heterostructures. For example, He *et al.*[5] demonstrated an electrically controlled perpendicular magnetization reversal in ultrathin Pd/Co multilayers in the presence of a static magnetic field by electrically reversing the uncompensated surface magnetization of an adjacent magnetoelectric antiferromagnet (0001)-Cr_2O_3 and thereby the polarity of the exchange bias field at the multilayer/Cr_2O_3 interface. Heron *et al.*[7] directly observed a voltage-driven in-plane net magnetization reversal in an exchange-coupled $Co_{0.9}Fe_{0.1}$/$BiFeO_3$ heterostructure, which was attributed to an electric-field-driven reversal of the canted magnetic moment on the surface of the $BiFeO_3$ film. Shiota *et al.*,[8] Kanai *et al.*,[9] and Grezes *et al.*[10] used voltage pulses to drive magnetization reversal in magnetic tunnel junctions in the presence of a static magnetic field, based on a temporal change in the magnetic easy axis (EA; via charge-mediated voltage control of magnetic anisotropy) in the magnetic-free layer. Ghidini *et al.*[11] exploited a similar scheme to explain their direct observation of voltage-driven reversal of local magnetization in the Ni electrode layer of a multilayer ceramic capacitor, considering that the magnetic EA is temporarily changed by fast strains resulting from fast ferroelectric domain switching. In spite of these intriguing experiments, voltage-driven reversal of uniform magnetization under zero external magnetic fields, which is favorable in many magnetoelectric device prototypes,[2,15] has not yet been demonstrated experimentally.

Computationally, there are several schemes[16–23] for achieving voltage-driven in-plane magnetization reversal under zero external magnetic fields mediated by strain[16,18,20,22,23] or exchange coupling.[17,21] By contrast, there is only one approach[24–27] for achieving voltage-driven perpendicular magnetization reversal under zero external magnetic fields, that is, using pulse-voltage-induced transient strains (through converse piezoelectric effect) to temporarily switch the perpendicular magnetic EA to the in-plane direction. Generally, a strain-mediated voltage-driven magnetization switching

[1]State Key Lab of New Ceramics and Fine Processing, School of Materials Science and Engineering, Tsinghua University, Beijing, China and [2]Department of Materials Science and Engineering, The Pennsylvania State University, University Park, PA, USA
Correspondence: Dr J-M Hu, Department of Materials Science and Engineering, N349 Millennium Science Complex, Materials Research Institute, The Pennsylvania State University, University Park, PA 16802, USA.
E-mail: juh34@psu.edu
or Professor C-W Nan, State Key Lab of New Ceramics and Fine Processing, School of Materials Science and Engineering, Tsinghua University, Beijing 100084, China.
E-mail: cwnan@tsinghua.edu.cn

(in-plane or perpendicular, 90° or 180°) involves the following four coupled dynamic processes as outlined in Hu et al.[2]: (i) establishment of the electric field in the piezoelectric, (ii) creation/release of strains, (iii) transfer of strain across the magnetic/piezoelectric interface, and (iv) strain-enabled magnetization switching in the magnet. However, existing computational studies of strain-mediated voltage-driven magnetization reversal (that is, 180° switching)[16,18–20,22–27] either did not consider the influence of the dynamics of process (ii) on process (iv)[16,18–20,22–26] or did not consider the influence of the stiffness damping coefficient of the piezoelectric when modeling the dynamics of process (ii).[27] Furthermore, most of these studies[16,18–20,22,24–27] did not consider the influence of thermal fluctuations on process (iv). Overall, a computational model that can be used for an accurate analysis of the speed of strain-mediated voltage-driven magnetization reversal is still lacking.

Here we perform an accurate analysis of the speed of piezostrain-mediated voltage-driven perpendicular magnetization reversal by combining finite-element analyses with micromagnetic phase-field simulations. This computational framework can be generally used to analyze the speed of piezostrain-enabled magnetization switching and magnetic domain-wall motion,[28] which critically determines the response time of the corresponding piezostrain-enabled spintronic and magnonic devices. Specifically, we computationally modeled the process (ii) by solving the elastodynamics equation in a three-dimensional finite-element model with the non-zero stiffness damping coefficient of the piezoelectric. The obtained temporally changing piezostrains are then fed into a micromagnetic phase-field model for simulating process (iv) with and without thermal fluctuations. The simulation results indicate that both the stiffness damping coefficient of the piezoelectric and the thermal fluctuations substantially affect the speed of reversal. Notably, in some cases, a non-zero stiffness damping of the piezoelectric can lead to a somewhat counterintuitive finding: a larger driving voltage decreases the speed of reversal.

Our analyses will also show that the time required by processes (i) and (iii) is negligible in the proposed model magnetic/piezoelectric heterostructure consisting of a 1.1-nm-thick elliptical amorphous $Co_{20}Fe_{60}B_{20}$ (CoFeB) nanomagnet fabricated on a 400-nm-thick poly-crystalline $Pb(Zr,Ti)O_3$ (PZT) thin film (see the schematic in Figure 1a). Note that experiments have confirmed the presence of perpendicular magnetic anisotropy in a 1.1-nm-thick amorphous CoFeB film.[29] This is consistent with the surface magnetization vector distribution (see the vector diagram in Figure 1a) obtained using a micromagnetic phase-field simulation (see Methods section) using experimentally measured material parameters (mostly from Yu et al.[29]) as the input.

The electrode structure shown in Figure 1a permits the generation of a nanosecond-long pulse of uniaxial in-plane piezostrains within the central ellipse region (that is, beneath the CoFeB) of the PZT film surface, as demonstrated by our elastodynamics simulations (see Methods section). According to a previously proposed scheme,[24] when the magnitude of the piezostrain is sufficiently large to reorient the perpendicular magnetic EA to the in-plane long axis, a full reversal of perpendicular magnetization can be achieved by controlling the pulse duration.

METHODS

Finite-element models
The equilibrium surface distributions of electric fields and piezostrains (in Figure 1) were obtained by steady-state analysis as implemented in the commercial COMSOL Multiphysics software package (COMSOL Group, Stockholm, Sweden). Details regarding obtaining such equilibrium distributions have been described in our previous work.[22]

The generation (release) of the local strain on the PZT film surface on application (removal) of a driving voltage was simulated using the time-dependent analysis module in COMSOL. The temporal evolution of piezostrains under a driving voltage pulse can be modeled by solving the following coupled equations:

$$\rho\frac{\partial^2 \mathbf{u}}{\partial t^2} = \nabla\cdot(\boldsymbol{\sigma} + \beta\frac{\partial[\mathbf{c}^E(\boldsymbol{\varepsilon} - \boldsymbol{\varepsilon}^0)]}{\partial t}), \tag{1a}$$

$$\boldsymbol{\sigma} = \mathbf{c}^E\boldsymbol{\varepsilon} - \mathbf{e}^T E, \tag{1b}$$

$$\boldsymbol{\varepsilon} = \left(\nabla\mathbf{u} + (\nabla\mathbf{u})^T\right)/2, \tag{1c}$$

$$\nabla\cdot\mathbf{D} = \nabla\cdot\left(e\boldsymbol{\varepsilon} + \kappa_0\kappa_r^S\mathbf{E}\right) = 0, \tag{1d}$$

where ρ is the density of PZT ($= 7.5\times10^3\,\mathrm{kg\,m^{-3}}$), $\mathbf{u}$ is the mechanical displacement, $\boldsymbol{\sigma}$ is the stress tensor, the stiffness-damping coefficient in Raleigh damping $\beta = (1/(f_r Q_m))$ (Nader et al.[30]) was calculated to be approximately 7 ps using the mechanical resonance frequency (f_r) of 2.2 GHz (obtained from our own finite-element analyses) and the mechanical quality factor (Q_m) of 65 (Ito and Uchino[31]) for a PZT film, $\boldsymbol{\varepsilon}$ is the total strain, $\mathbf{c}^E$ is the elastic stiffness constant tensor of the PZT measured under constant electric field and E is the spatially variant electric field, $\mathbf{e}^T$ denotes the transpose of the piezoelectric stress coefficient tensor e, D is the electric displacement, κ_0 is the vacuum permittivity and κ_r^S denotes the relative dielectric permittivity tensor measured under mechanically clamped boundary conditions.

A cuboid-shaped space domain in COMSOL Multiphysics, with dimensions of 3000 nm (length)×3000 nm (width)×400 nm (thickness) is used to describe the PZT thin film. The space domain was discretized using free tetrahedral meshes with quadratic shape functions. The elastodynamic equation (see Equation 1a) was solved by combining the Multifrontal Massively Parallel Sparse direct Solver with the implicit time-dependent backward differentiation formulas solver,[22] under periodic boundary conditions for $\mathbf{u}$ imposed on the lateral surfaces of the space domain. In the model, the voltage applied on the two top electrodes (Figure 1) increases linearly from 0 V to the maximum value within 70 ps (which is an experimentally achievable rise time[8]) at the rate of 5 ps per time step. For simplicity, the model assumes that electrostatic equilibrium (Equation 1d) is achieved at each time step. In practice, the time required to achieve the electrostatic equilibrium is related to the resistance–capacitance (RC) delay time (see Discussion section below).

Micromagnetic phase-field model
The influence of piezostrains on magnetization dynamics (shown in Figure 2) in a patterned nanomagnet was simulated using a previously developed micromagnetic phase-field model,[24] which is now upgraded to a fully parallel micromagnetic simulation package called μ-Pro Mag. For model verification, we used μ-Pro Mag to solve all five standard micromagnetic problems outlined by the micromagnetic modeling activity group (μMag) (http://www.ctcms.nist.gov/~rdm/mumag.org.html) at the National Institute of Standards and Technology. The results produced by μ-Pro Mag (which can be accessed through the link in http://www.ems.psu.edu/~chen/package/example.html) are in good agreement with those obtained by existing micromagnetic simulation packages, including both OOMMF[32] and MuMax3.[33] The unique feature of our model (μ-Pro Mag) is that it fully couples local magnetization dynamics with elasticity, as will be discussed below.

In our model, the temporal evolution of the local magnetization vector $\mathbf{M}$ is described by the Landau–Lifshitz–Gilbert equation:

$$\left(1 + \alpha^2\right)\frac{\partial\mathbf{M}}{\partial t} = -\gamma_0(\mathbf{M}\times\mathbf{H}_{eff}) - \frac{\gamma_0\alpha}{M_s}\mathbf{M}\times(\mathbf{M}\times\mathbf{H}_{eff}), \tag{2}$$

where γ_0 and α denote the gyromagnetic ratio and the Gilbert damping coefficient, respectively. M_s denotes the saturation magnetization of the 1.1-nm-thick amorphous CoFeB. The effective magnetic field is given by $\mathbf{H}_{eff} = \mathbf{H}_{therm} - (1/\mu_0)(\delta F_{tot}/\delta\mathbf{M})$. Here $H_{i,therm}$ ($i = x, y, z$) is a stochastic magnetic field that couples magnetization dynamics with random thermal fluctuations at ambient temperature,[34] has a zero statistical average and can be
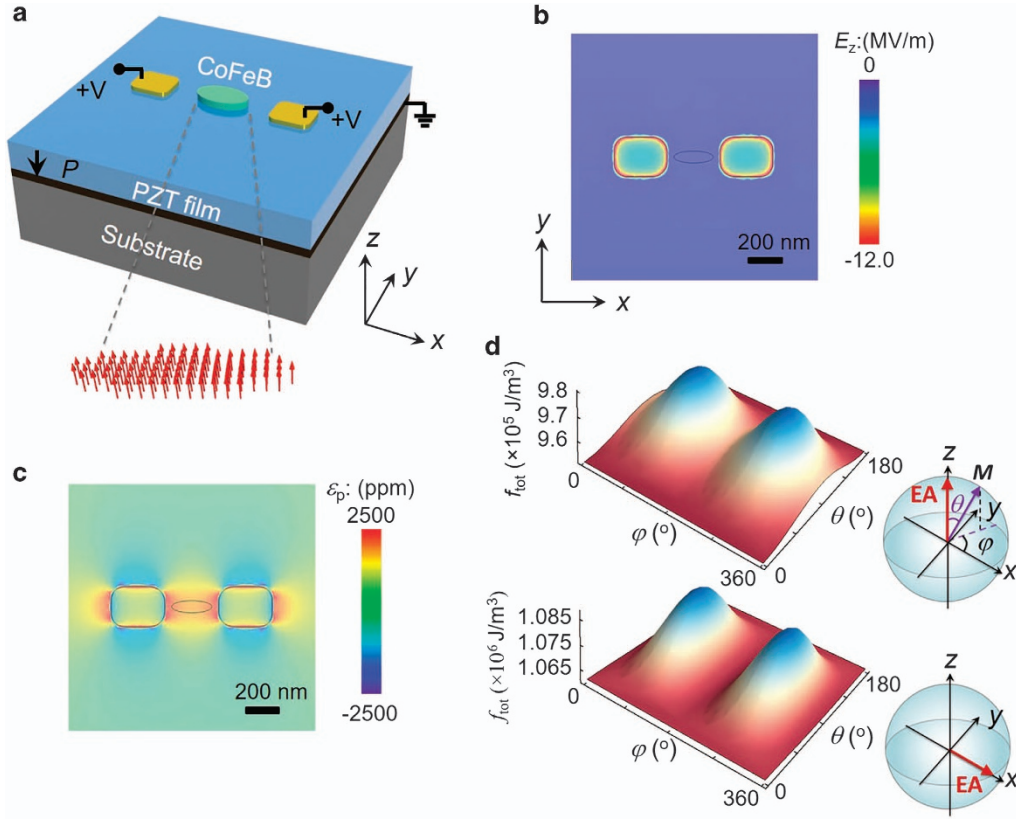
Figure 1 (a) Schematic of a multiferroic heterostructure consisting of an amorphous elliptical CoFeB nanomagnet deposited on a polycrystalline PZT thin film. The vector plot shows the distribution of local magnetizations (indicated by arrows) in CoFeB after application of a strong static magnetic field along the $+z$ direction. Distributions of (b) out-of-plane electric field (E_z) and (c) in-plane piezostrain ($\varepsilon_p = \varepsilon_{xx} - \varepsilon_{yy}$) on the surface of PZT, where a static 0.90-V voltage is applied to the two top electrodes. (d) Landscape of total free energy density of the CoFeB nanomagnet with dimensions of $300 \times 90 \times 1.1$ nm^3 without (top) and with (bottom) the applied static 0.9-V voltage. Corresponding orientations of the magnetic easy axis (EA) are indicated in the insets.

described as[33]

$$\langle H_{i,\text{therm}}(\text{step}) \rangle = 0, H_{i,\text{therm}}(\text{step}) = \eta_i(\text{step})\sqrt{\frac{2\alpha k_B T}{\mu_0 M_s \gamma_0 \Delta V \Delta t}}, \quad (3)$$

where μ_0 denotes the vacuum permeability, k_B is the Boltzmann constant, T is the Kelvin temperature, ΔV ($= \Delta x \times \Delta y \times \Delta z$) is the real volume of a discretized grid (in the unit of m^3), and Δt denotes the real time (in the unit of seconds) for each numerical time step. η_i ($i = x, y, z$) is one of three components of a random vector η. The value of η_i obeys the standard normal distribution and changes independently at each time step.

F_{tot} is the total free energy of the amorphous CoFeB nanodisk, which can be expressed as

$$F_{\text{tot}} = \int_V (f_{\text{ms}} + f_{\text{exch}} + f_{\text{elastic}} + f_{\text{interface}}) dV, \quad (4)$$

where f_{ms}, f_{exch}, f_{elastic} and $f_{\text{interface}}$ are the magnetostatic, exchange, elastic and magnetic interface energy densities, respectively. The magnetic interface energy density $f_{\text{interface}} = K_s(1 - m_z^2)/d$ corresponds to the perpendicular magnetic anisotropy experimentally observed in a 1.1-nm-thick CoFeB film,[29] where K_s is the magnetic interface energy density and d is the thickness of the magnet. Mathematical expressions and numerical solutions of the f_{exch} and f_{ms} can be found elsewhere.[35] The elastic energy density f_{elastic} can be expressed by

$$
\begin{aligned}
f_{\text{elastic}} &= \tfrac{1}{2}c_{ijkl}\left(\varepsilon_{ij} - \varepsilon_{ij}^0\right)\left(\varepsilon_{kl} - \varepsilon_{kl}^0\right), \\
\varepsilon_{ij}^0 &= \tfrac{3}{2}\lambda_s\left(m_i^2 - \tfrac{1}{3}\right), i = j, \\
\varepsilon_{ij}^0 &= \tfrac{3}{2}\lambda_s m_i m_j, i \neq j, \\
\varepsilon_{ij} &= \overline{\varepsilon_{ij}} + \varepsilon_{ij}^{\text{inhom}},
\end{aligned}
\quad (5)
$$

where c_{ijkl} denotes the elastic stiffness coefficient of the amorphous CoFeB, ε_{ij}^0 describes the spontaneous deformation of a magnetized body due to magnetostriction and λ_s denotes the saturation magnetostriction; based on Khachaturyan's theory of microelasticity,[36] the total strain ε_{ij} was written as the sum of a homogeneous strain $\overline{\varepsilon_{ij}}$ and an inhomogeneous strain $\varepsilon_{ij}^{\text{inhom}}$, describing the average and local deformation in a sample, respectively. The source of the average strain $\overline{\varepsilon_{ij}}$ in the CoFeB magnet is the average local piezostrain on the PZT film surface $\overline{\varepsilon_p}$ ($= \overline{\varepsilon_{xx}} - \overline{\varepsilon_{yy}}$), see the elliptical region in Figure 1c. Once $\overline{\varepsilon_{ij}}$ is known, $\varepsilon_{ij}^{\text{inhom}}$ can be obtained by solving the mechanical equilibrium equation $\nabla \cdot \left[c_{ijkl}\varepsilon_{kl}^{\text{inhom}} - c_{ijkl}\left(\varepsilon_{kl}^0 - \overline{\varepsilon_{kl}}\right)\right] = 0$. During evolution of the magnetization, $\varepsilon_{ij}^{\text{inhom}}$ was constantly updated by solving this equation.

Three-dimensional discrete grids of $160\Delta x \times 55\Delta y \times 25\Delta z$ with real grid sizes $\Delta x = \Delta y = 2.0$ nm and $\Delta z = 0.275$ nm are used to describe the three-phase system of the bottom PZT film ($= 17\Delta z$), its overlaying CoFeB nanomagnet ($= 4\Delta z = 1.1$ nm) and the gas phase (including the top $4\Delta z$ layers and those surrounding the CoFeB in the middle four layers). The real grid sizes (namely, Δx, Δy and Δz) are all smaller than the exchange length[37] of CoFeB ($l_{\text{ex}} = \sqrt{A/(0.5\mu_0 M_s^2)} \approx 4.4$ nm). The shape of the CoFeB ellipse nanomagnet is described using the shape function $(x - 80\Delta x)^2/(75\Delta x)^2 + (y - 55\Delta y/2)^2/(75\Delta x \times r)^2 - 1 = 0$ with the axial ratio r. The effect of the axial ratio on magnetization switching is studied by varying the grid size or grid numbers. The material parameters of CoFeB used for the simulations, including the saturated magnetization, elastic stiffness coefficients, saturation magnetostriction, gyromagnetic ratio, Gilbert damping coefficient and exchange constant of CoFeB nanomagnet, were collected from the literature and are as follows: $M_s = 1.25 \times 10^6$ A m^{-1} (Yu *et al.*[29]); $c_{11} = 218.1$ GPa, $c_{12} = 93.46 \times 10^{11}$ GPa and $c_{44} = 62.32$ GPa (Hindmarch *et al.*[38] and Wang *et al.*[39]); $\lambda_s = 3.7 \times 10^{-5}$ (Yu *et al.*[29]); $\gamma_0 = 1.82 \times 10^{11}$ Hz T^{-1} (Yu *et al.*[29]);
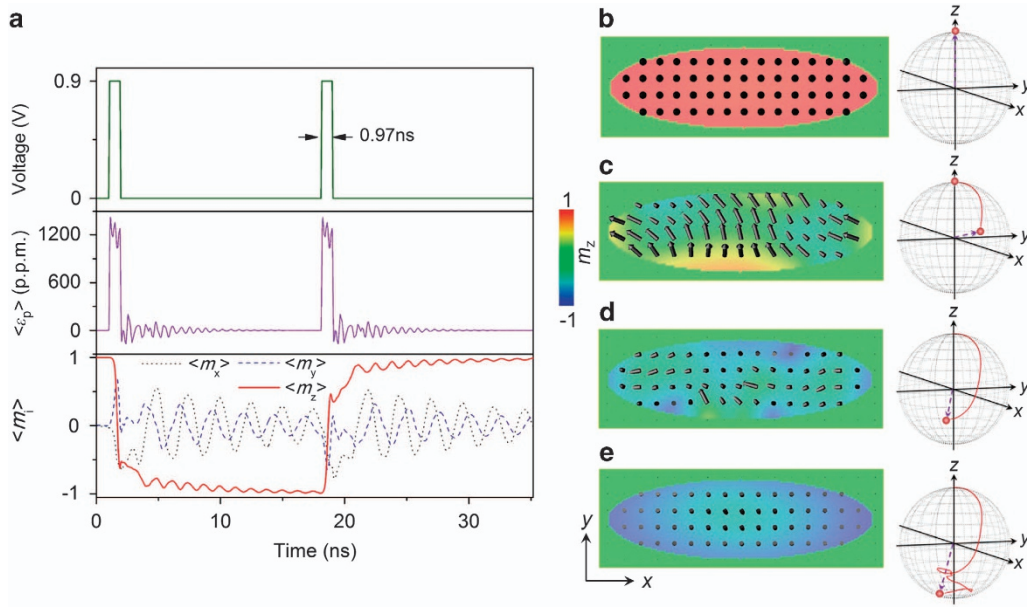
Figure 2 (**a**) A square-wave voltage pulse with a duration of 0.97 ns (including a 0.07 ns rise and fall time) and amplitude of 0.9 V (the top panel) generates dynamically changing strains ε_p in the CoFeB region on the PZT film surface (middle panel shows its average $<\varepsilon_\mathrm{p}>$). Such dynamically changing strains further enable a complete 180° perpendicular magnetization reversal repeatedly; see the temporal evolution of the average magnetization component $<m_i>$ ($i=x$, y, z) in the bottom panel. (**b–e**) Snapshots of the surface magnetization distributions during the perpendicular magnetization reversal at 1, 1.70, 1.90 and 5.36 ns, where $<m_z>=0.99$, 0.02, -0.62 and -0.90, respectively. The color bar indicates the value of local magnetization component m_z, while the arrows denote the orientations of local magnetization vectors. The corresponding three-dimensional trajectories of magnetization reversal at these different time stages are shown on the right.

$\alpha=0.04$ (Yu *et al.*[29]); and $A_\mathrm{ex}=1.9\times10^{-11}$ J m^{-1}.[40] The magnetic interface energy density K_s is approximately 1.05 mJ m^{-2}. The real-time span ($\Delta t\approx0.07$ ps) is correlated with the numerical time step ($\Delta\tau=0.02$) through $\Delta t=\Delta\tau(1+\alpha^2)/(\gamma_0 M_\mathrm{S})$.

Linking the finite-element model to the micromagnetic phase-field model

As mentioned above, the homogeneous strain $\overline{\varepsilon_{ij}}$ in the micromagnetic phase-field model (Equation 5) is equal to the average local piezostrain on the PZT film surface $\overline{\varepsilon_\mathrm{p}}$. The temporal evolution of $\overline{\varepsilon_\mathrm{p}}$ can be obtained from the time-dependent finite-element model (Equations 1a–d). Notably, $\overline{\varepsilon_{ij}}$ in the micromagnetic phase-field model will be updated whenever $\overline{\varepsilon_\mathrm{p}}$ changes. This feature links the finite-element model to the micromagnetic phase-field model. Specifically, the data for the temporally changing $\overline{\varepsilon_\mathrm{p}}$ were fed to the $\overline{\varepsilon_{ij}}$ every 5 ps (that is, the voltage rise/fall rate) when the voltage is rising to its nominal maximum value or falling to zero. At the rest of the time stages, $\overline{\varepsilon_\mathrm{p}}$ exhibits a relatively small variation with time. This allows us to feed the $\overline{\varepsilon_\mathrm{p}}$ data with a longer interval (every 10 ps herein) to reduce the computational cost.

RESULTS

The elliptical-cylinder-shaped CoFeB has dimensions of 300 nm (full length of long-axis) × 90 nm (full length of short axis) × 1.1 nm (thickness). For these dimensions, the energy barrier ($=f_\mathrm{b}V_\mathrm{m}$, where f_b represents the potential barrier and V_m is the volume of the magnet) between the perpendicular magnetization and an in-plane long-axis magnetization reaches 40 $k_\mathrm{B}T$, which is the minimum required for ensuring a thermally stable initial perpendicular magnetization.[41] Although a larger energy barrier will lead to a higher thermal stability of the initially perpendicular magnetization, a larger strain will then be required to switch the initially perpendicular magnetic EA to the in-plane long-axis (see Supplementary Figure S1a). Variation of the thickness of the nanomagnet will modulate such an energy barrier through the modulation of both the magnetic interface energy and the

magnetic stray field (or demagnetization) energy.[42,43] On the other hand, variation of the in-plane dimension of the nanomagnet will modulate the energy barrier through the modulation of the magnetic stray field energy only. The effects of the in-plane aspect ratio and the thickness of the nanomagnet on the thermal stability factor ($=f_\mathrm{b}V_\mathrm{m}/k_\mathrm{B}T$) are shown in Supplementary Figure S1b. It is shown that thickness (d) must not be larger than a critical value $d_{cr}=K_\mathrm{s}/\left[0.5\mu_0 M_\mathrm{S}^2(N_{33}-N_{11})+(40k_\mathrm{B}T/V_m)\right]$, where N_{33} and N_{11} are the analytically calculated demagnetization factors of an elliptical cylinder.[44] Specifically, we obtain $d\leqslant d_{cr}=1.1$ nm for in-plane dimensions of 300×90 nm^2.

We used the electrode design (see Figure 1a) proposed by Cui *et al.*[45] to obtain locally uniaxial in-plane piezostrains on the surface of a polycrystalline piezoelectric film by applying out-of-plane driving voltages. Figures 1b and c show the equilibrium surface distributions of the local out-of-plane electric field (E_z) and local piezostrain along the in-plane long axis ($\varepsilon_\mathrm{p}=\varepsilon_{xx}-\varepsilon_{yy}$) in response to the driving voltage of 0.9 V, respectively. As shown in Figure 1b, local electric fields concentrate near the sharp edges of the top electrodes, but even the largest local E_z (21.9 MV m^{-1}) is smaller than the reported dielectric breakdown field of a 400-nm-thick PZT film (25 MV m^{-1}, Moazzami *et al.*[46]). In practice, the concentrated electric fields are expected to be smaller in magnitude because of the rough edges. Such an inhomogeneous electric field induces locally tensile piezostrains within the region of the CoFeB ellipse of, on average, approximately 1213 p.p.m. Because of the shear-lag effect,[47] these piezostrains cannot be completely transferred to the CoFeB even when assuming a tightly bonded interface without slipping (see the simulated nonuniform piezostrain distribution in Supplementary Information S2). The simulations indicate that the actual uniaxial piezostrain experienced by the CoFeB is approximately 1034 p.p.m. (strain transfer efficiency of ~85%). However, such strain is still sufficient to reorient the

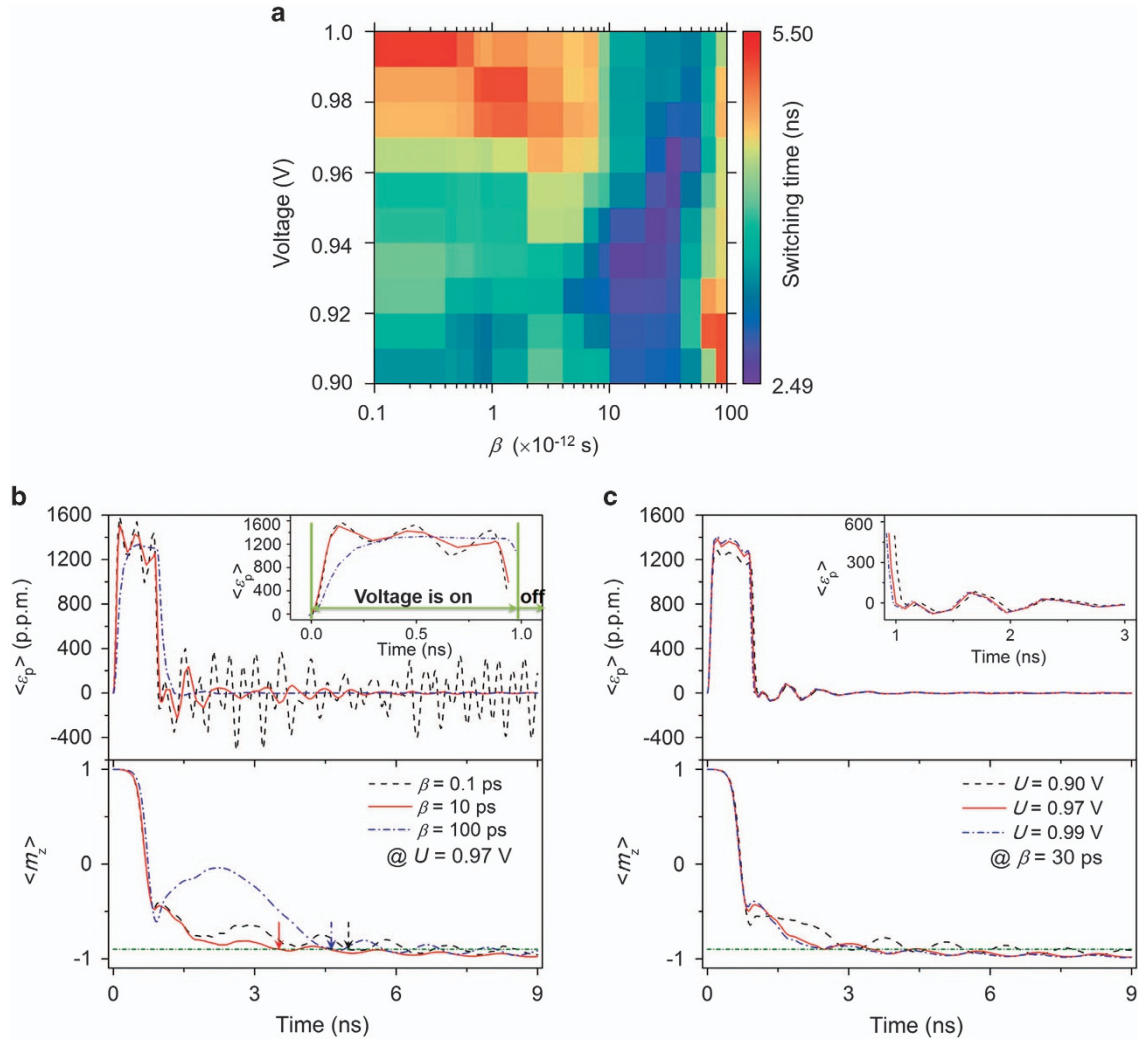**Figure 3** (**a**) Diagram showing the perpendicular magnetization switching time as a function of the amplitude of applied voltage pulse (U) and the stiffness-damping coefficient (β) of the PZT film. (**b**, **c**) Temporal evolution of the average strain in the CoFeB region on the PZT film surface $<\varepsilon_\mathrm{p}>$ and the average magnetization component $<m_z>$ during the magnetization reversal, where $\beta=0.1$, 10 and 100 ps, $U=0.97$ V in (**b**) while $U=0.90$, 0.97 and 0.99 V and $\beta=30$ ps in (**c**) The insets show the enlarged profiles of $<\varepsilon_\mathrm{p}>$ before and after turning off the voltage in (**b**, **c**), respectively. Note that the voltage is turned off when $<m_z>$ reaches its negative minimum in all cases. The arrows mark the time when $<m_z>$ reaches -0.90 (indicated by the horizontal dashed dotted line in the bottom panels of (**b**, **c**).

initially perpendicular magnetic EA to the in-plane x axis. The upper and lower panels of Figure 1d display the phase-field model profiles of the total magnetic-free energy density of the CoFeB nanomagnet without and with the applied voltages, respectively. It can be seen that the application of uniaxial in-plane piezostrains along the x axis ($\varepsilon_\mathrm{p}=\varepsilon_{xx}-\varepsilon_{yy}$) can change the global energy minima and hence the magnetic EA from the initial out-of-plane z axis ($\theta=0°$ and 180°) to the in-plane x axis ($\theta=90°$ and $\varphi=0°/180°/360°$).

Figure 2a shows a dynamic piezostrain-mediated 180° perpendicular magnetization reversal driven by a square-shaped voltage pulse with a duration of 0.97 ns, including 70 ps for the voltage rise and fall between 0 and 0.9 V (see top panel). Dynamic piezostrains in response to such a voltage pulse obtained from the finite-element simulations (see Methods section) are shown in the middle panel of Figure 2a. Turning the voltage on at 1 ns almost instantly switches the initially perpendicular magnetic EA to the in-plane long axis x owing to the rapidly rising strain (that is, the strain rises to its maximum value within 0.14 ns). As a result, the perpendicular magnetization

(see Figure 2b) starts to precess around the x axis and crosses the horizontal plane at 1.7 ns (see Figure 2c). If the voltage is not turned off, the magnetization vector will eventually align largely along the x axis (that is, a 90° switching, see Supplementary Figure S3). However, turning the voltage off when the z component of the average magnetization ($<m_z>$) is negative will enable a full magnetization reversal. For example, after the voltage is switched off when $<m_z>$ reaches its negative maximum (at 1.90 ns, see also Figure 2d), the residual strain quickly vanishes with oscillation. Consequently, the perpendicular magnetic EA re-appears, and $<m_z>$ relaxes to the nearby global energy minima (namely, $-z$ axis) in a deterministic manner, completing a perpendicular magnetization reversal (see also Figure 2e). In total, a purely voltage-driven perpendicular magnetization reversal ($<m_z>$ changing to approximately -1) occurs within 4.36 ns, including the $>90°$ precessional switching driven by the 0.97-ns voltage pulse and the subsequent 3.39-ns magnetization relaxation toward the re-appeared perpendicular magnetic EA. Such a voltage-driven perpendicular reversal is nonvolatile

because the perpendicular magnetic anisotropy provides a potential barrier separating two energetically degenerate states at $<m_z> = +1$ and -1 ($\theta = 0°$ and $180°$, see the barrier profile in Figure 1d). Such a reversal is also repeatable: application of another identical voltage pulse can switch the magnetization back to the $+z$ direction.

We now discuss how the magnitude of the applied voltage pulse (U) and the stiffness-damping coefficient (β) of PZT thin film influence the speed of perpendicular magnetization reversal. A diagram showing the total switching time as a function of U (vertical axis) and β is calculated through the combination of finite-element analyses and phase-field simulations, as shown in Figure 3a. The switching time was recorded when the initial upward magnetization rotates to a downward state where $<m_z> = -0.90$, as indicated by the horizontal short dashed dotted line in the bottom panels of Figures 3b and c. Diagrams calculated using criteria of $<m_z> = -0.92$ and $<m_z> = -0.94$ show the same trend as this diagram and can be found in Supplementary Figure S5. We discuss this diagram with respect to the following two aspects.

First, under the same U, the switching time first decreases and then increases with increasing β. When β is small (for example, 0.1 ps), strain relaxation after the removal of the voltage is slow (see the top panel of Figure 3b), such that the relaxation of $<m_z>$ to the global energy minima at $-z$ axis is slow as well. Thus the switching time is relatively long (see the bottom panel of Figure 3b). A moderate β (for example, 10 ps) leads to faster strain relaxation and hence faster magnetization relaxation. Therefore, the switching time decreases. However, a relatively large (for example, 100 ps) β would lead to a relatively large initial residual strain after the removal of the voltage (see the inset in the top panel of Figure 3b), which would slow down the magnetization relaxation. Thus the switching time increases to some extent.

Second, we found that the variation trends of switching time under the same β but with increasing U are complex. When β is small (for example, $\beta = 0.1$ ps), the switching time increases with increasing U. This seems to be counterintuitive: a larger U leads to a larger piezostrain, which further leads to a faster magnetization precession, meaning that the $<m_z>$ would reach its negative maximum more rapidly. However, the subsequent magnetization relaxation under zero voltage becomes slower because of the increasing magnitude of the residual strains. Thus the overall switching time becomes longer (see Supplementary Figure S4a). Let us consider the other extreme with relatively large β (for example, $\beta = 100$ ps). In this case, residual strains decrease rapidly to zero after the voltage is turned off (Supplementary Figure S4b), so that the switching time is mainly determined by how fast the $<m_z>$ would reach its first negative maximum rather than by the subsequent magnetization relaxation. As discussed above, the former process is faster under a larger U (larger piezostrain), while the latter process is faster under a smaller U (smaller residual strain). Therefore, the switching time decreases with increasing U. The competition between these two processes is more evident under a moderate β (for example, $\beta = 30$ ps), where the switching time first decreases and then increases with increasing U. Notably, the shortest switching time (≈ 2.5 ns) appears under a moderate U (0.97 V) and a moderate β ($= 30$ ps), where the magnitudes of both the piezostrain (when the voltage is on) and residual strain (when the voltage is off) are moderate. The corresponding temporal evolutions of $<m_z>$ and the piezostrain are shown in Figure 3c.

DISCUSSION
Switching speed
Using computational modeling of the temporal strain evolution in the PZT film on application of a 0.97- ns-duration voltage pulse and the magnetization dynamics under such a dynamically changing strain, we demonstrated a magnetization reversal time as low as 2.5 ns.
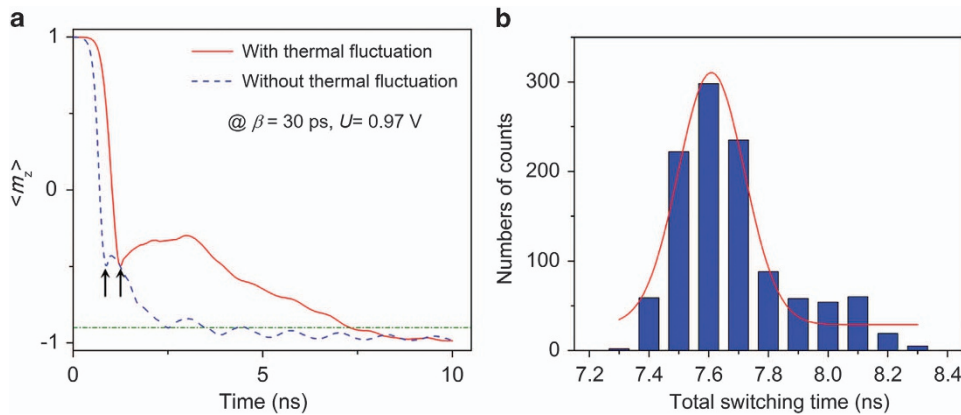
Figure 4 (**a**) Piezostrain-mediated voltage-driven perpendicular magnetization reversal (where $<m_z>$ changes from about $+1$ to -0.9, marked by the short dashed dot line), with and without room temperature (300 K) thermal fluctuations, with $\beta = 30$ ps and $U = 0.97$ V. (**b**) Corresponding statistic distribution of the switching time from $<m_z> \approx +1$ to $<m_z> = -0.90$ with room temperature (300 K) thermal fluctuation, obtained by repeating the simulations 1100 times under the same conditions. The results can be fitted using a normal distribution (see the solid line), yielding a mean value of 7.61 ns for the switching time.

Table 1 Comparison of existing and emerging schemes for achieving perpendicular magnetization reversal

	Current-induced magnetization reversal		Voltage-driven magnetization reversal	
	STT mediated[53,54]	SOT mediated[55–57]	Charge mediated[10,52]	Strain mediated (this work)
Switching time (ns)	1–10	0.3–1	0.5–1	2.5
Area energy dissipation per switching (J m^{-2})	30.2–90.3	6.72–30.1	3.1–14.2	0.05

Abbreviations: SOT, spin-orbit-torque; STT, spin-transfer-torque.

Furthermore, the times required to establish/release electric fields on application of the voltage (~3.4 ps) and to transfer the piezostrain from the PZT surface to the top CoFeB (~0.2 ps) are both negligible in the present structure. The former time is related to the RC delay (that is, $t_{RC} \approx R \times C$) during the PZT charging/discharging, using a typical R of about $100\,\Omega$[48] and a capacitance ($C \approx P_r S/U \approx 34$ fF). Here the remnant ferroelectric polarization of PZT film with 400-nm thickness P_r is 150 fC μm^{-2},[46] the area of top electrodes S is about $0.22\,\mu m^2$ and the amplitude of the voltage pulse U is 0.97 V. The time required for the piezostrain transfer (t_p) was calculated by $t_p = d/v$,[41] using the CoFeB thickness (d) of 1.1 nm and a mechanical wave propagation velocity in the CoFeB (v) of about 4800 m s^{-1}.[22] Taken together, the factors reduce the overall time required to achieve a piezostrain-mediated voltage-driven magnetization reversal to 2.5 ns in the present structure.

Now we further discuss the influence of room-temperature (300 K) thermal fluctuations on the switching speed. As shown in Figure 4a, the obtained switching time is approximately 7.3 ns with thermal fluctuations, compared with 2.5 ns without thermal fluctuations. This is mainly because the thermal fluctuations retard the relaxation of the magnetization to its new equilibrium (where $<m_z> = -1$). The relaxation process starts on turning off the voltage at the negative maximum of $<m_z>$ (indicated by the black arrows in Figure 4a). Furthermore, simulations incorporating thermal fluctuations were repeated for 1100 times under the same conditions to obtain a statistical distribution of the switching times. As shown in Figure 4b, the switching time ranges from 7.3 to 8.3 ns. Notably, the results can be fitted using a normal distribution with the mean switching time of 7.61 ns (see the solid curve in Figure 4b). Such a statistical distribution of the switching times is related to the normal distribution of the random vector η in Equation 3.

Energy consumption and dissipation

For the present PZT film and electrode design, the energy consumption per switching (~16 fJ per bit) is given by $E_{con} = 0.5 P_r S U$ (Hu et al.[41]), with an area energy consumption ($=E_{con}/S$) of about 0.07 J m^{-2}. The energy dissipation of PZT (~10.6 fJ) per switching is calculated using $E_{dis} = 0.5\pi \tan(\delta) E_{con}$,[49] where the dielectric loss tan (δ) depends on the frequey of the applied voltage pulse ($f \approx 1/(2.49+16.12$ ns$) \approx 53.7$ MHz) and is approximately 0.42 at this frequency.[50] The corresponding area energy dissipation ($=E_{dis}/S$) in the PZT is calculated as about 0.05 J m^{-2}. Note that the dielectric loss can be smaller in practice because a unipolar voltage pulse rather than a bipolar a.c. voltage is employed in the present design, which could further reduce the energy dissipation. Furthermore, the energy dissipation from the damped magneitization precession can be esitmated by $E_{dis,m} = V_m \frac{\alpha M_s}{\gamma_0} \int_0^{t_{sw}} \left(\frac{dm}{dt}\right)^2 dt$,[51] where V_m is the volume of the CoFeB nanomagnet. Using a switching time (t_{sw}) of 2.5 ns, $E_{dis,m}$ is calculated to be 6.6×10^{-5} fJ per switching, which is negligible compared with E_{dis}, the energy dissipation in the PZT.

Table 1 compares the speed and the area energy dissipation of the present piezostrain-mediated voltage-driven perpendicular magnetization reversal to those of charge-mediated voltage-driven[10,52] and current-driven[53–57] perpendicular magnetization reversal mediated by spin-transfer-torque[53,54] or spin-orbit-torque.[55–57] As can be seen from the data presented in Table 1, the switching speed of the present scheme is comparable to those of the current-driven schemes but is slower than that of the charge-mediated voltage-driven scheme where a static magnetic field is typically required. Furthermore, the area energy dissipation in the present scheme is around two orders of magnitude smaller than that of the charge-mediated voltage-driven scheme and is about three orders of magnitude smaller than those of the current-driven schemes. Optimization of materials selection can further enhance the switching speed and reduce the areal energy dissipation.

Summary

To summarize, we used finite-element analyses to calculate the dynamically changing piezostrain on the surface of a piezoelectric PZT thin film upon the application of a sub-ns voltage pulse and used a micromagnetic phase-field model to evaluate the speed of such dynamic piezostrain-enabled perpendicular magnetization reversal in the top magnetostrictive CoFeB ultrathin nanomagnet. Compared with the conventional micromagnetic simulations, the micromagnetic phase-field model enables the simulation of the coupling between magnetization dynamics and elasticity, that is, the back-action of the magnetization dynamics on the local strain state is considered; see the text below Equation 5. Compared with the previous modeling studies of piezostrain-mediated voltage-driven perpendicular magnetization reversal,[24–26] this work addresses how the dynamically changing piezostrain and notably the stiffness damping in the piezoelectric phase influence the magnetization dynamics and thereby the switching speed. In particular, our results show that the switching speed is highest (switching time ~ 2.5 ns) when both the amplitude of the piezostrain pulse (voltage) and the stiffness-damping coefficient of the piezoelectric are moderately large (Figure 3a). It was also shown that room-temperature (300 K) thermal fluctuations can significantly reduce the switching speed, yet the switching time (~7.6 ns) still remains well below 10 ns. Compared with the perpendicular magnetization reversal enabled by other schemes (see Table 1), the present piezostrain-mediated voltage-driven scheme shows a moderate switching speed but significantly lower energy dissipation. The same analyses of the switching speed can be adopted to evaluate the response time of other piezostrain-enabled spintronic and magnetic devices.

CONFLICT OF INTEREST

The authors declare no conflict of interest.

1 Hu, J.-M., Duan, C.-G., Nan, C.-W. & Chen, L.-Q. Understanding and designing magnetoelectric heterostructures guided by computation: progresses, remaining questions, and perspectives. NPJ Comput. Mater. 3, 18 (2017).
2 Hu, J. M., Chen, L. Q. & Nan, C. W. Multiferroic heterostructures integrating ferroelectric and magnetic materials. Adv. Mater. 28, 15–39 (2016).
3 Taniyama, T. Electric-field control of magnetism via strain transfer across ferromagnetic/ferroelectric interfaces. J. Phys. Condens. Matter 27, 504001 (2015).
4 D'Souza, N., Fashami, M. S., Bandyopadhyay, S. & Atulasimha, J. Experimental clocking of nanomagnets with strain for ultralow power Boolean logic. Nano Lett. 16, 1069–1075 (2016).
5 He, X., Wang, Y., Wu, N., Caruso, A. N., Vescovo, E., Belashchenko, K. D., Dowben, P. A. & Binek, C. Robust isothermal electric control of exchange bias at room temperature. Nat. Mater. 9, 579–585 (2010).
6 Skumryev, V., Laukhin, V., Fina, I., Martí, X., Sánchez, F., Gospodinov, M. & Fontcuberta, J. Magnetization reversal by electric-field decoupling of magnetic and ferroelectric domain walls in multiferroic-based heterostructures. Phys. Rev. Lett. 106, 057206 (2011).

7 Heron, J. T., Bosse, J. L., He, Q., Gao, Y., Trassin, M., Ye, L., Clarkson, J. D., Wang, C., Liu, J., Salahuddin, S., Ralph, D. C., Schlom, D. G., Íñiguez, J., Huey, B. D. & Ramesh, R. Deterministic switching of ferromagnetism at room temperature using an electric field. *Nature* **516**, 370–373 (2014).

8 Shiota, Y., Nozaki, T., Bonell, F., Murakami, S., Shinjo, T. & Suzuki, Y. Induction of coherent magnetization switching in a few atomic layers of FeCo using voltage pulses. *Nat. Mater.* **11**, 39–43 (2012).

9 Kanai, S., Yamanouchi, M., Ikeda, S., Nakatani, Y., Matsukura, F. & Ohno, H. Electric field-induced magnetization reversal in a perpendicular-anisotropy CoFeB-MgO magnetic tunnel junction. *Appl. Phys. Lett.* **101**, 122403 (2012).

10 Grezes, C., Ebrahimi, F., Alzate, J. G., Cai, X., Katine, J. A., Langer, J., Ocker, B., Amiri, P. K. & Wang, K. L. Ultra-low switching energy and scaling in electric-field-controlled nanoscale magnetic tunnel junctions with high resistance-area product. *Appl. Phys. Lett.* **108**, 012403 (2016).

11 Ghidini, M., Pellicelli, R., Prieto, J., Moya, X., Soussi, J., Briscoe, J., Dunn, S. & Mathur, N. Non-volatile electrically-driven repeatable magnetization reversal with no applied magnetic field. *Nat. Commun.* **4**, 1453 (2013).

12 Yang, S. W., Peng, R. C., Jiang, T., Liu, Y. K., Feng, L., Wang, J. J., Chen, L. Q., Li, X. G. & Nan, C. W. Non-volatile 180° magnetization reversal by an electric field in multiferroic heterostructures. *Adv. Mater.* **26**, 7091–7095 (2014).

13 Shirahata, Y., Shiina, R., González, D. L., Franke, K. J. A., Wada, E., Itoh, M., Pertsev, N. A., Dijken, S. V. & Taniyama, T. Electric-field switching of perpendicularly magnetized multilayers. *NPG Asia Mater.* **7**, e198 (2015).

14 Chen, A. T., Zhao, Y. G., Li, P.S., Zhang, X., Peng, R. C., Huang, H., Zou, L., Zheng, X., Zhang, S., Miao, P., Lu, Y., Cai, J. & Nan, C. W. Angular dependence of exchange bias and magnetization reversal controlled by electric-field-induced competing anisotropies. *Adv. Mater.* **28**, 391–391 (2016).

15 Hu, J. M., Nan, T. X., Sun, N. X. & Chen, L. Q. Multiferroic magnetoelectric nanostructures for novel device applications. *MRS Bull.* **40**, 728–735 (2015).

16 Novosad, V., Otani, Y., Ohsawa, A., Kim, S. G., Fukamichi, K., Koike, J., Maruyama, K., Kitakami, O. & Shimada, Y. Novel magnetostrictive memory device. *J. Appl. Phys.* **87**, 6400 (2000).

17 Fechner, M., Zahn, P., Ostanin, S., Bibes, M. & Mertig, I. Switching magnetization by 180° with an electric field. *Phys. Rev. Lett.* **108**, 197206 (2012).

18 Roy, K., Bandyopadhyay, S. & Atulasimha, J. Binary switching in a 'symmetric' potential landscape. *Sci. Rep.* **3**, 3038 (2013).

19 Peng, R. C., Wang, J. J., Hu, J. M., Chen, L. Q. & Nan, C. W. Electric-field-driven magnetization reversal in square-shaped nanomagnet-based multiferroic heterostructure. *Appl. Phys. Lett.* **106**, 142901 (2015).

20 Wang, J. J., Hu, J. M., Ma, J., Zhang, J. X., Chen, L. Q. & Nan, C. W. Full 180º magnetization reversal with electric fields. *Sci. Rep.* **4**, 07507 (2014).

21 Wang, J. J., Hu, J. M., Peng, R. C., Gao, Y., Shen, Y., Chen, L. Q. & Nan, C. W. Magnetization reversal by out-of-plane voltage in BiFeO₃-based multiferroic heterostructures. *Sci. Rep.* **5**, 10459 (2015).

22 Peng, R. C., Hu, J. M., Momeni, K., Wang, J. J., Chen, L. Q. & Nan, C. W. Fast 180° magnetization switching in a strain-mediated multiferroic heterostructure driven by a voltage. *Sci. Rep.* **6**, 27561 (2016).

23 Biswas, A. K., Bandyopadhyay, S. & Atulasimha, J. Complete magnetization reversal in a magnetostrictive nanomagnet with voltage-generated stress: a reliable energy-efficient non-volatile magneto-elastic memory. *Appl. Phys. Lett.* **105**, 072408 (2014).

24 Hu, J. M., Yang, T. N., Wang, J. J., Huang, H. B., Zhang, J. X., Chen, L. Q. & Nan, C. W. Purely electric-field-driven perpendicular magnetization reversal. *Nano Lett.* **15**, 616–622 (2015).

25 Li, X., Carka, D., Liang, C.-Y., Sepulveda, A. E., Keller, S. M., Amiri, P. K., Carman, G. P. & Lynch, C. S. Strain-mediated 180° perpendicular magnetization switching of a single domain multiferroic structure. *J. Appl. Phys.* **118**, 014101 (2015).

26 Yi, M., Xu, B. X. & Shen, Z. G. 180º magnetization switching in nanocylinders by a mechanical strain. *Extreme Mech. Lett.* **3**, 66–71 (2015).

27 Wang, Q. C., Li, X., Liang, C.-Y., Barra, A., Domann, J., Lynch, C., Sepulveda, A. & Carman, G. Strain-mediated 180° switching in CoFeB and Terfenol-D nanodots with perpendicular magnetic anisotropy. *Appl. Phys. Lett.* **110**, 102903 (2017).

28 Hu, J.-M., Yang, T. N., Momeni, K., Cheng, X. X., Chen, L., Lei, S. M., Zhang, S. J., Trolier-McKinstry, S., Gopalan, V., Carman, G. P., Nan, C.-W. & Chen, L.-Q. Fast magnetic domain-wall motion in a ring-shaped nanowire driven by a voltage. *Nano Lett.* **16**, 2341–2348 (2016).

29 Yu, G. Q., Wang, Z., Abolfath-Beygi, M., He, C., Li, X., Wong, K. L., Nordeen, P., Wu, H., Carman, G. P., Han, X., Alhomoudi, I. A., Amiri, P. K. & Wang, K. L. Strain-induced modulation of perpendicular magnetic anisotropy in Ta/CoFeB/MgO structures investigated by ferromagnetic resonance. *Appl. Phys. Lett.* **106**, 072402 (2015).

30 Nader, G., Silva, E. & Adamowski, J. Effective damping value of piezoelectric transducer determined by experimental techniques and numerical analysis. *ABCM Symp. Ser. Mechatronics* **1**, 271–279 (2004).

31 Ito, Y. & Uchino, K. *Piezoelectricity. Wiley Encyclopedia of Electrical and Electronics Engineering* Vol. 16, 479–481 (John Wiley & Sons, Inc.: New York, USA, 1999).

32 Donahue, M. J. & Porter, D. G. *OOMMF User's Guide, Version 1.0,* Interagency Report NISTIR 6376 (National Institute of Standards and Technology: Gaithersburg, MD, USA, 1999).

33 Vansteenkiste, A., Leliaert, J., Dvornik, M., Helsen, M., Garcia-Sanchez, F. & Waeyenberge, B. V. The design and verification of MuMax3. *AIP Adv.* **4**, 107133 (2014).

34 Brown, W. F. Thermal fluctuations of a single-domain particle. *Phys. Rev.* **130**, 1677–1686 (1963).

35 Zhang, J. X. & Chen, L. Q. Phase-field microelasticity theory and micromagnetic simulations of domain structures in giant magnetostrictive materials. *Acta Mater.* **53**, 2845–2855 (2005).

36 Khachaturyan, A. G. *Theory of Structural Transformations in Solids* (Dover Publications, 2008).

37 Abo, G. S., Hong, Y.-K., Park, J., Lee, J., Lee, W. & Choi, B.-C. Definition of magnetic exchange length. *IEEE Trans. Magn.* **49**, 4937–4939 (2013).

38 Hindmarch, A. T., Rushforth, A. W., Campion, R. P., Marrows, C. H. & Gallagher, B. L. Origin of in-plane uniaxial magnetic anisotropy in CoFeB amorphous ferromagnetic thin films. *Phys. Rev. B* **83**, 212404 (2011).

39 Wang, D. X., Nordman, C., Qian, Z., Daughton, J. M. & Myers, J. Magnetostriction effect of amorphous CoFeB thin films and application in spin-dependent tunnel junctions. *J. Appl. Phys.* **97**, 10C906 (2005).

40 Sato, H., Yamanouchi, M., Miura, K., Ikeda, S., Koizumi, R., Matsukura, F. & Ohno, H. CoFeB thickness dependence of thermal stability factor in CoFeB/MgO perpendicular magnetic tunnel junctions. *IEEE Magn. Lett* **3**, 3000204 (2012).

41 Hu, J. M., Li, Z., Chen, L. Q. & Nan, C. W. High-density magnetoresistive random access memory operating at ultralow voltage at room temperature. *Nat. Commun.* **2**, 553 (2011).

42 Pertsev, N. A. Converse magnetoelectric effect via strain-driven magnetization reorientations in ultrathin ferromagnetic films on ferroelectric substrates. *Phys. Rev. B* **92**, 014416 (2015).

43 Hu, J.-M., Nan, C.-W. & Chen, L.-Q. Size-dependent electric voltage controlled magnetic anisotropy in multiferroic heterostructures: Interface-charge and strain comediated magnetoelectric coupling. *Phys. Rev. B* **83**, 134408 (2011).

44 Beleggia, M., Graef, M. D., Millev, Y. T., Goode, D. A. & Rowlands, G. Demagnetization factors for elliptic cylinders. *J. Phys. D Appl. Phys.* **38**, 3333 (2005).

45 Cui, J. Z., Hockel, J. L., Nordeen, P. K., Pisani, D. M., Liang, C. Y., Carman, G. P. & Lynchet, C. S. A method to control magnetism in individual strain-mediated magnetoelectric islands. *Appl. Phys. Lett.* **103**, 232905 (2013).

46 Moazzami, R., Hu, C. & Shepherd, W. Electrical characteristics of ferroelectric PZT thin films for DRAM applications. *IEEE Trans. Electron. Devices* **39**, 2044–2049 (1992).

47 Liang, C. Y., Keller, S. M., Sepulveda, A. E., Sun, W. Y., Cui, J., Lynch, C. S. & Carman, G. P. Electrical control of a single magnetoelastic domain structure on a clamped piezoelectric thin film—analysis. *J. Appl. Phys.* **116**, 123909 (2014).

48 Fashami, M. S., Roy, K., Atulasimha, J. & Bandyopadhyay, S. Magnetization dynamics, Bennett clocking and associated energy dissipation in multiferroic logic. *Nanotechnology* **22**, 155201 (2011).

49 www.noliac.com/tutorials/dynamic-actuators/heat-dissipation/. Accessed January 2017.

50 Foster, F. S., Ryan, L. K. & Turnbull, D. H. Characterization of lead zirconate titanate ceramics for use in miniature high-frequency (20-80 MHz) transducers. *IEEE Trans. Ultrason. Ferroelect. Freq. Control* **38**, 446 (1991).

51 Tiercelin, N., Dusch, V., Giordano, S., Klimov, A., Preobrazhensky, V. & Pernod, P. in *Nanomagnetic and Spintronic Devices for Energy-Efficient Memory and Computing* 221–257 (John Wiley & Sons, Ltd., 2016).

52 Amiri, P. K., Alzate, J. G., Cai, X. Q., Ebrahimi, F., Hu, Q., Wong, K., Grezes, C., Lee, H., Yu, G., Li, X., Akyol, M., Shao, Q., Katine, J. A., Langer, J., Ocker, B. & Wang, K. L. Electric-field-controlled magnetoelectric RAM: progress, challenges, and scaling. *IEEE Trans. Magn.* **51**, 1–7 (2015).

53 Wang, K. L., Alzate, J. G. & Amiri, P. K. Low-power non-volatile spintronic memory: STT-RAM and beyond. *J. Phys. D Appl. Phys.* **46**, 074003 (2013).

54 Patel, R., Guo, X., Guo, Q., Ipek, E. & Friedman, E. G. Reducing switching latency and energy in STT-MRAM caches with field-assisted writing. *IEEE Trans. Very Large Scale Integr. (VLSI) Syst.* **24**, 129–138 (2016).

55 Prenat, G., Jabeur, K., Vanhauwaert, P., Pendina, G. D., Oboril, F., Bishnoi, R., Ebrahimi, M., Lamard, N., Boulle, O., Garello, K., Langer, J., Ocker, B., Cyrille, M.-C., Gambardella, P., Tahoori, M. & Gaudin, G. Ultra-fast and high-reliability SOT-MRAM: from cache replacement to normally-off computing. *IEEE Trans. Multiscale Comp. Syst.* **2**, 49–60 (2016).

56 Garello, K., Avci, C. O., Miron, I. M., Baumgartner, M., Ghosh, A., Auffret, S., Boulle, O., Gaudin, G. & Gambardella, P. Ultrafast magnetization switching by spin-orbit torques. *Appl. Phys. Lett.* **105**, 212402 (2014).

57 Oboril, F., Bishnoi, R., Ebrahimi, M. & Tahoori, M. B. Evaluation of hybrid memory technologies using SOT-MRAM for on-chip cache hierarchy. *IEEE Trans. Comput. Aided Des. Integr. Circuits Syst.* **34**, 367–380 (2015).

Supplementary Information accompanies the paper on the NPG Asia Materials website (http://www.nature.com/am)